

Supplementary Information For Highly-Oriented Atomically Thin Ambipolar MoSe₂ Grown by Molecular Beam Epitaxy

Ming-Wei Chen^{1,2}, Dmitry Ovchinnikov^{1,2}, Sorin Lazar³, Michele Pizzochero⁴, Michael Brian Whitwick¹, Alessandro Surrente⁵, Michał Baranowski^{5,6}, Oriol Lopez Sanchez^{1,2}, Philippe Gillet⁴, Paulina Plochocka⁵, Oleg V. Yazyev⁴, Andras Kis^{1,2*}

¹Electrical Engineering Institute, École Polytechnique Fédérale de Lausanne (EPFL), CH-1015 Lausanne, Switzerland

²Institute of Materials Science and Engineering, École Polytechnique Fédérale de Lausanne (EPFL), CH-1015 Lausanne, Switzerland

³FEI Electron Optics, 5600 KA Eindhoven, The Netherlands

⁴Institute of Physics, École Polytechnique Fédérale de Lausanne (EPFL), CH-1015 Lausanne, Switzerland

⁵Laboratoire National des Champs Magnétiques Intenses CNRS-UGA-UPS-INSA, 143 avenue de Rangueil, Toulouse, France

⁶Department of Experimental Physics, Faculty of Fundamental Problems of Technology, Wrocław University of Science and Technology, Wybrzeże Wyspińskiego 27, 50-370 Wrocław Poland

*Correspondence should be addressed to: Andras Kis, andras.kis@epfl.ch

1. XPS survey and core-level of Ga 3d and As 3d

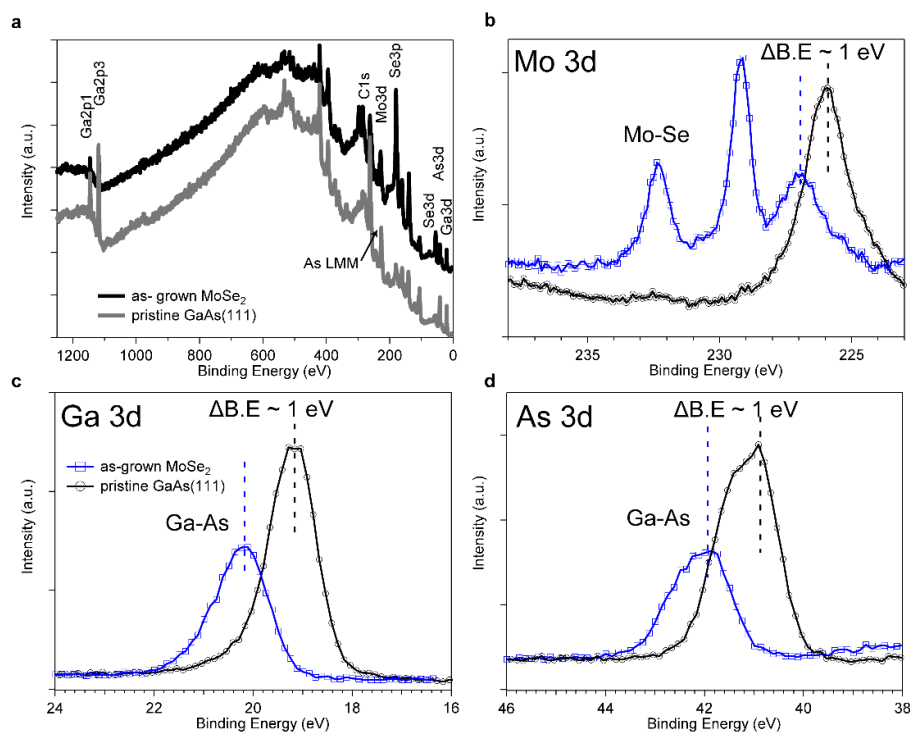


Figure S1. XPS survey comparison and charge-transfer effect in core-level spectra. (a) Survey spectrum of MoSe₂ and reference GaAs(111). (b) comparison of Mo 3d, (c) Ga 3d and (d) As 3d core-level spectra in XPS between as-grown MoSe₂ and pristine GaAs(111).

The survey spectra of the same sample from Figure 1e and 1f in main text are shown in Figure S1a. The ASLMM peak at ~ 277 eV is evident in the survey spectra. The comparison between as-grown MoSe₂ and pristine GaAs(111)B in different core-level spectral regions is shown in Figure S1b-d. After MoSe₂ growth, all the peaks shift toward higher binding energy

by ~ 1 eV, while the peak shapes remain the same. The results indicate that the electrons from the substrate were transferred to the as-grown MoSe₂ and that no intermediate compound formed during the growth. The as-grown sample and the pristine GaAs(111)B were separately prepared but were from the same wafer and following the same pretreatment protocol. Even though they were characterized *ex-situ*, the ambient exposure was minimized during transportation and no detectable oxidation was observed.

2. Observation of MoSe₂ grown at 470°C

MoSe₂ grown using GaAs as the substrate can be transferred onto other substrates or even suspended for TEM studies. On Figure S2 we show an optical image of a nominally monolayer MoSe₂ film transferred from the GaAs substrate to a silicon substrate with a 270 nm thick SiO₂ layer. The film was transferred by coating the GaAs substrate with the grown MoSe₂ layer with PMMA and delaminating from the surface using a 30% KOH solution.

An overall statistical analysis is performed on low-magnification HAADF-STEM images. The original image is shown in Figure S3a and the different layers are denoted. Figure S3b shows the result of stacking two color-coded IFFT (inverse Fast Fourier transform) images together with the original image. The different colors thus represent thickness-correlated grain orientation: ML (A) is dark red, ML (B) dark blue, BL (A+A) as red, BL (B+B) light blue, and BL (A+B) magenta. Summary and the pie chart of BL orientations are shown in Figure S3c and d, respectively. The results show that the exposed ML (A) and ML

(B) are randomly distributed with equivalent percentages. In BL regions, BL (A+B) is prevailing ($>70\%$ of the area), BL (A+A) has 30% area, and BL (B+B) is rare. Other two high-

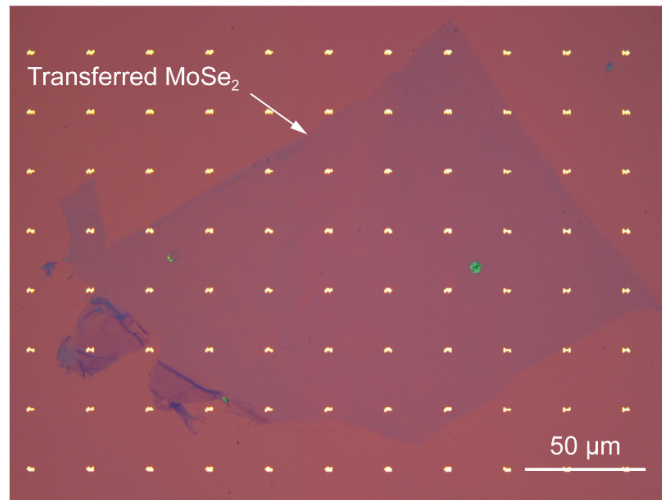


Figure S2. Optical micrograph of a transferred MoSe₂ film. The film was transferred using KOH-based wet transfer from the GaAs substrate used for growth onto a silicon substrate with a 270 nm thick SiO₂ layer.

magnification HAADF-STEM images and corresponding color-coded images are shown in Figure S3e and f. (The original HAADF-STEM image of Figure S3e is shown in Figure 2b in the main text.) The results imply that as the two misoriented domains meet, they do not stop growing and do not form a visible grain boundary. Instead, one domain prefers to grow over another one through the edge while still preserving its own orientation. The dynamic growth mechanism is illustrated in Figure S3g with the perspective and side view.

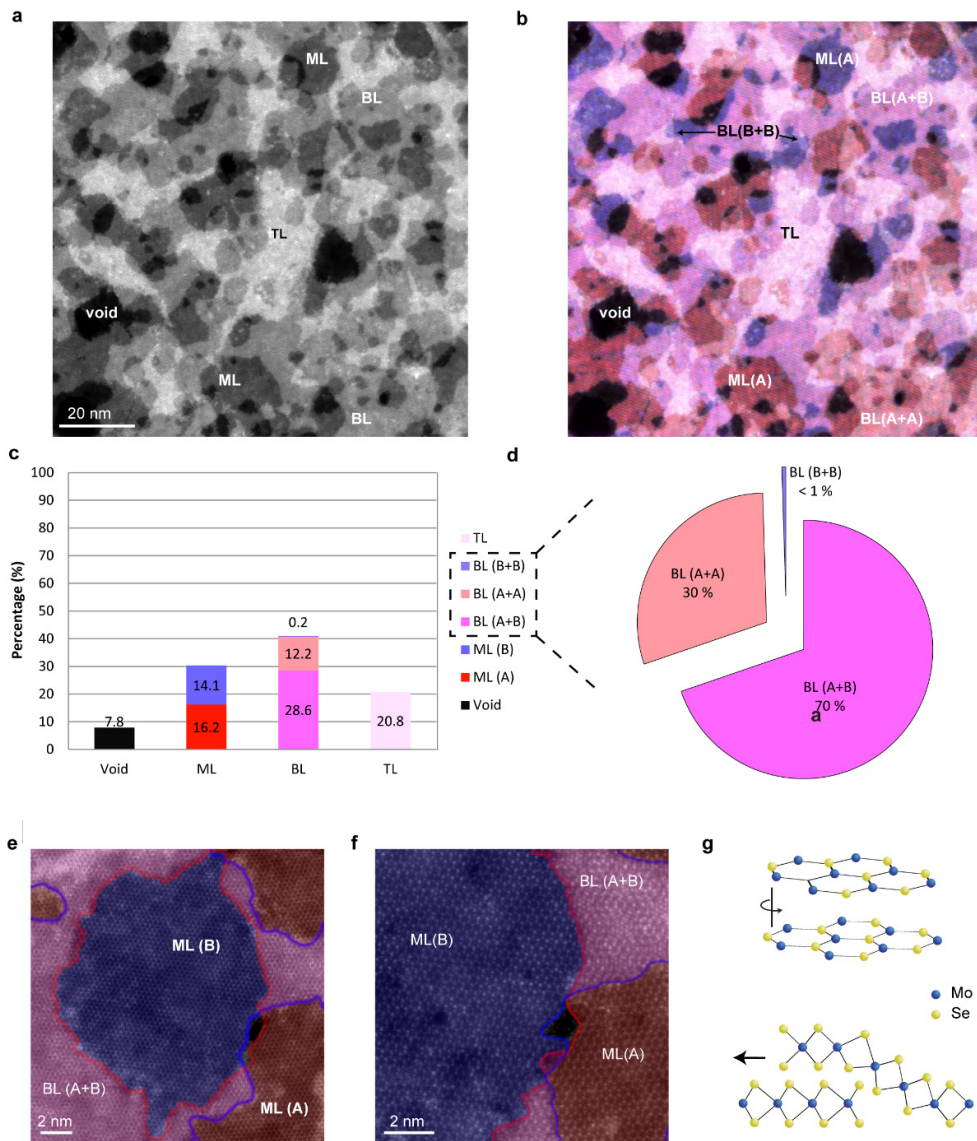


Figure S3. Grain orientation in MoSe₂ grown at 470 °C. (a) A HAADF-STEM image and (b) stacking of color-coded IFFT images and the original image. The different color contrasts represent thickness-correlated relative orientations: ML (A), ML (B), BL (A+B), BL (A+A), BL (B+B) and TL. (c) Percentage of thickness-correlated orientation and (d) the pie chart of BL orientation angles. (e) (f) Stacking results of color-coded IFFT images (red as ML domain A and blue as ML domain B) and original images. Boundaries are highlighted for easier observation. (e) Illustrated overgrowth mechanism at the boundary region from perspective and side view. The arrow indicates the growth direction of the overlay.

3. Formation energy of single-oriented and misoriented films by density functional theory calculations

3.1 Methods and models

Our first-principles calculations are based on the density functional theory (DFT) formalism,¹ as implemented in the SIESTA code.² The exchange and correlation effects are included through the generalized gradient approximation (GGA) of Perdew, Burke and Ernzerhof (PBE)³ while we account for the van der Waals interactions by means of the Grimme dispersion correction.⁴ Core electrons are replaced by norm-conserving Troullier-Martins pseudopotentials whereas valence electrons are expanded in a linear combination of double- ζ plus polarization (DZP) basis set in conjunction with a mesh cutoff of 300 Ry. A Γ -centered k-mesh following the Monkhorst-Pack scheme is adopted for the integration over the reciprocal space; such a mesh consists of $12 \times 12 \times 1$ k-points per GaAs(111)B unit cell, properly rescaled in order to preserve the grid spacing while considering supercells. Geometries are relaxed until the maximum force component acting on each atom converges to 0.04 eV/Å, while cell constants are kept fixed to the values of pristine GaAs(111)B. A vacuum region larger than 25 Å is included to avoid interaction between periodic images. Spin-orbit coupling is considered only in the calculation of the electronic band structure. Within this computational setup, we obtained lattice parameters of $a_{GaAs} = 4.06$ Å and $a_{MoSe2} = 3.35$ Å for GaAs(111)B and single-layer MoSe₂, respectively, in good agreement with experimental values of 4.00 Å and 3.29 Å.

To model superlattices of ML MoSe₂ on GaAs(111)B, we place MoSe₂ supercells of up to (8×8) on top of four slabs of GaAs(111)B in such a way that the strain is minimized, *i.e.* smaller than a reasonable value of 10 %. Within this strategy, we obtained 5 models of the same orientation of MoSe₂ and GaAs lattices (see Table S1) and 10 models for supercells that involve relative rotations between the MoSe₂ and GaAs lattices (see Table S2). These models contain from 84 up to 531 atoms. Twist angle θ is defined as the difference between angles θ' and θ'' shown in Figure S3.

In order to investigate the stability of single-layer MoSe₂ on GaAs(111)B, for each model we compute the formation energy per formula unit as:

$$E_{form} = (E_{GaAs+MoSe2} - E_{GaAs} - n \times \mu_{Mo} - 2 \times n \times \mu_{Se}) / n$$

with $E_{GaAs+MoSe2}$ being the total energy of the model under investigation, E_{GaAs} the total energy of isolated GaAs(111)B substrate, n the number of Mo atoms in the MoSe₂ supercell, μ_{Mo} the chemical potential of molybdenum and μ_{Se} the chemical potential of selenium. As reference systems for the chemical potentials, we choose the bulk Mo *bcc* crystal and the isolated Se₈ molecule. This equation accounts for the formation energy of single-layer MoSe₂ once the GaAs(111)B substrate is already formed, in analogy with the real situation.

Compared to the free-standing case, when MoSe₂ is placed on the GaAs(111)B surface, two effects should be expected. On the one hand, the unfavorable biaxial strain of MoSe₂, due to the adjustment of the lattice constants of the monolayer to the one of the substrate, defined as

$$\varepsilon = (a_{GaAs} - a_{MoSe2}) / a_{GaAs} \%$$

where positive (negative) values of ε signal tensile (compressive) lattice strain. Strain effects mostly result from matching two incommensurate systems in a simulation supercell of reasonable size. It is thus crucial to understand the contribution of strain to the overall formation energy computed for our models. On the other hand, we have the favorable van der Waals interactions between MoSe₂ and GaAs(111)B. We estimate these two contributions introducing two quantities, E_{strain} and E_{inter} , respectively, defined as:

$$E_{\text{strain}} = E_{\text{MoSe2-frozen}} - E_{\text{MoSe2}}$$

$$E_{\text{inter}} = E_{\text{GaAs+MoSe2}} - E_{\text{GaAs-frozen}} - E_{\text{MoSe2-frozen}}$$

with being $E_{\text{MoSe2-frozen}}$ ($E_{\text{GaAs-frozen}}$) the total energy of unrelaxed MoSe₂ matched to the GaAs(111)B substrate, and E_{MoSe2} being the total energy of relaxed MoSe₂. These two quantities describe the energy necessary to strain a MoSe₂ monolayer and the energy released once the matched MoSe₂ and GaAs(111)B are stacked one on top of each other, respectively.

3.2 Results and discussion

First, we investigate the models without relative rotation between the two lattices. In Table S1 the five structures considered are listed. For these models, the strain modulus of MoSe₂ ranges from about 1 % to 9 %. The most stable configuration is the *d* model, where a (5 × 5) MoSe₂ lattice placed on a (4 × 4) GaAs(111)B substrate leads to a formation energy of −3.70 eV/ f.u. In order to analyze the stability of oriented superlattices, in Figure S4 we show both E_{strain} and E_{inter} . Comparing these models, one can notice that E_{strain} is smallest in *b* and *c* models whereas E_{inter} is more favorable in *a* and *b* ones. Overall, the stability of a superlattice is driven by the competition between these two energy contributions, *i.e.* their sum, that turns out to be minimal for the *d* model, for which the formation energy is indeed the lowest.

Next, we consider lattices with relative rotation (see Figure S4), whose models and corresponding formation energies are listed in Table S2: some of these structures are compatible with the experimentally observed twist angle of 7.5° (*e.g.* *A*, *G* and *L*). As discussed in the previous section, these models are built in such a way that the strain is minimized. However, the MoSe₂ lattice strain is reduced to 0.1 – 0.2 % when a twist angle between the monolayer and the substrate is introduced, therefore indicating that almost perfect lattice matching takes place. As a consequence, the E_{strain} is small (a few meV at most) making it hardly visible in the Figure S5. In general, formation energies of all models that include rotation are about −3.77 eV/f.u., irrespectively of the twist angle considered. For the rotated models, we additionally determined the adhesion energy, *i.e.* the adsorption energy per unit area (Table S2). We found values ranging from 39 to 51 meV/Å². Björkman et al. estimated van der Waals bonding in layered compounds to be ~20 meV/Å², irrespectively of the electronic structure of the material.⁵ Though within the same order of magnitude, our adhesion energies of MoSe₂ / GaAs(111)B heterostructures are larger. The reason for this can be traced back to the dangling bonds at the GaAs(111)B surface, responsible for more reactive behavior of such substrate towards binding monolayer MoSe₂, as opposed to more inert substrates such as graphene, h-BN or transition metal dichalcogenides investigated in Ref. 5. Such dangling bonds contribute covalent character to the resulting interaction, thereby increasing the values of adhesive energies.

Comparing the stability of both configurations, we found that a slightly larger stability occurs when a twist between the two lattices is considered. The reason for this is twofold: on one hand, relative rotation strongly reduces the strain in single-layer MoSe₂; on the other hand, E_{inter} in configurations with relative rotation are some tens of meV more favorable than in the oriented one, *i.e.* a slightly stronger binding of the monolayer with the substrate is present. Overall, formation energies of oriented and rotated superlattices are very similar – with the latter more favourable only by about 60 meV/f.u. – suggesting that both cases are likely to form due to the minor difference in energy that emerges from our simulations.

Finally, the charge transfer at the MoSe₂ /GaAs(111)B interface for the single-oriented structure is presented in the Figure S6. The charge density of both isolated MoSe₂ and GaAs(111)B are obtained first, and the charge density of the entire system is subtracted from the isolated ones. What remains is the charge density difference between MoSe₂ and

GaAs(111)B. As a result, a very small amount of positive charge ($\sim 0.001 e/\text{\AA}^3$) is located in the interlayer region, demonstrating the weak coupling at the interface between MoSe₂ and GaAs(111)B.

Model	(n × n)	(m × m)	Number of atoms	<i>a</i> (Å)	ε (%)	E_{form} (eV / f.u.)
<i>a</i>	(4 × 4)	(3 × 3)	84	12.19	−9.08	−3.020
<i>b</i>	(5 × 5)	(4 × 4)	139	16.25	−3.02	−3.710
<i>c</i>	(6 × 6)	(5 × 5)	208	20.31	1.03	−3.522
<i>d</i>	(7 × 7)	(6 × 6)	291	24.37	3.91	−3.392
<i>e</i>	(8 × 8)	(7 × 7)	388	28.43	6.08	−3.221

Table S1. Investigated models of MoSe₂ / GaAs(111)B lattices without relative rotation. (n × n) and (m × m) indicate the size of the supercells of MoSe₂ and GaAs(111)B, respectively, *a* the lattice constant, ε the strain in MoSe₂ and E_{form} the formation energy.

Model	[n ₁ , n ₂]	[m ₁ , m ₂]	Number of Atoms	<i>a</i> (Å)	θ (deg)	ε (%)	E_{form} (eV / f.u.)	E_{adh} (meV / Å ²)
<i>A</i>	[7, 4]	[7, 2]	361	26.64	11.52	0.15	−3.764	39
<i>B</i>	[7, 4]	[2, 7]	361	26.64	26.70	0.15	−3.776	47
<i>C</i>	[5, 8]	[7, 4]	531	32.24	19.84	−0.23	−3.776	48
<i>D</i>	[8, 5]	[7, 4]	531	32.24	1.95	−0.23	−3.771	40
<i>E</i>	[3, 4]	[4, 2]	103	14.65	22.69	0.27	−3.778	51
<i>F</i>	[3, 5]	[4, 3]	160	17.71	17.48	−0.15	−3.772	40
<i>G</i>	[3, 5]	[3, 4]	160	17.71	4.31	−0.15	−3.771	40
<i>H</i>	[6, 2]	[2, 5]	177	18.61	19.84	−0.23	−3.777	48
<i>I</i>	[2, 6]	[2, 5]	177	18.61	1.95	−0.23	−3.771	40
<i>L</i>	[4, 3]	[4, 2]	109	14.65	9.52	0.27	−3.764	40

Table S2. Investigated models of MoSe₂ / GaAs(111)B lattices with relative rotation. [n₁, n₂] and [m₁, m₂] indicate the periodicity of MoSe₂ and GaAs(111)B, respectively, *a* the lattice constant, θ the twist angle, ε the strain in MoSe₂, E_{form} the formation energy and E_{adh} the adhesive energy.

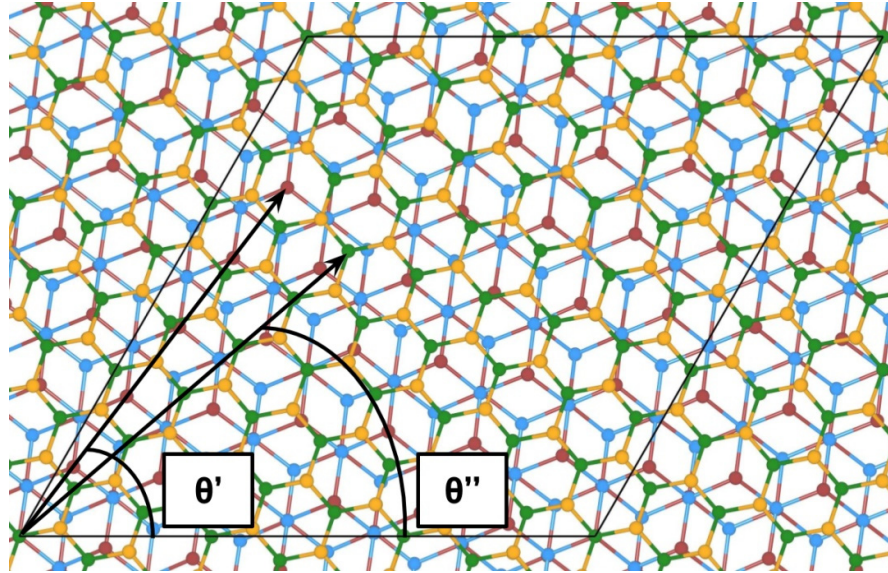


Figure S4. Example of rotated lattice of MoSe₂ on GaAs(111)B (model A according to Table S2): red, blue, green and orange balls represent As, Ga, Mo and Se atoms, respectively. Twist angle θ is defined as the difference between θ' and θ'' .

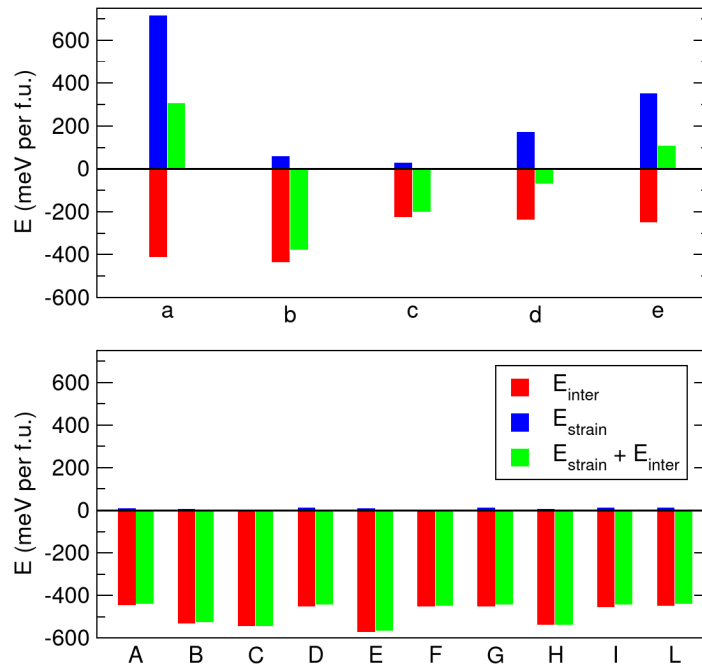


Figure S5. E_{inter} , E_{strain} and their sum for models without (upper panel) and with (lower panel) a twisting angle. Models are labeled according to Tables S1 and S2.

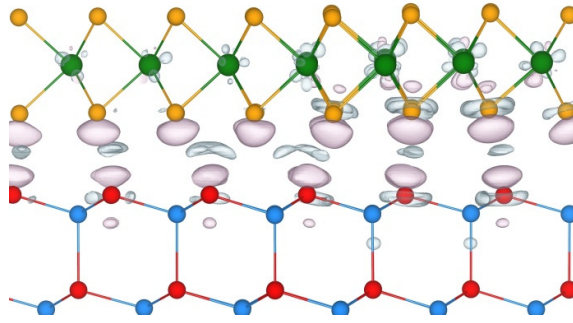


Figure S6. Charge transfer at the interface of MoSe₂ / GaAs(111)B for the most stable single-oriented structure (model *b* according to Table S1). Grey (pink) clouds represent positive (negative) charge density and isosurfaces are set to 0.001 e/Å³.

4. SHG and spectroscopic characterization of ML MoSe₂ grown at 530°C

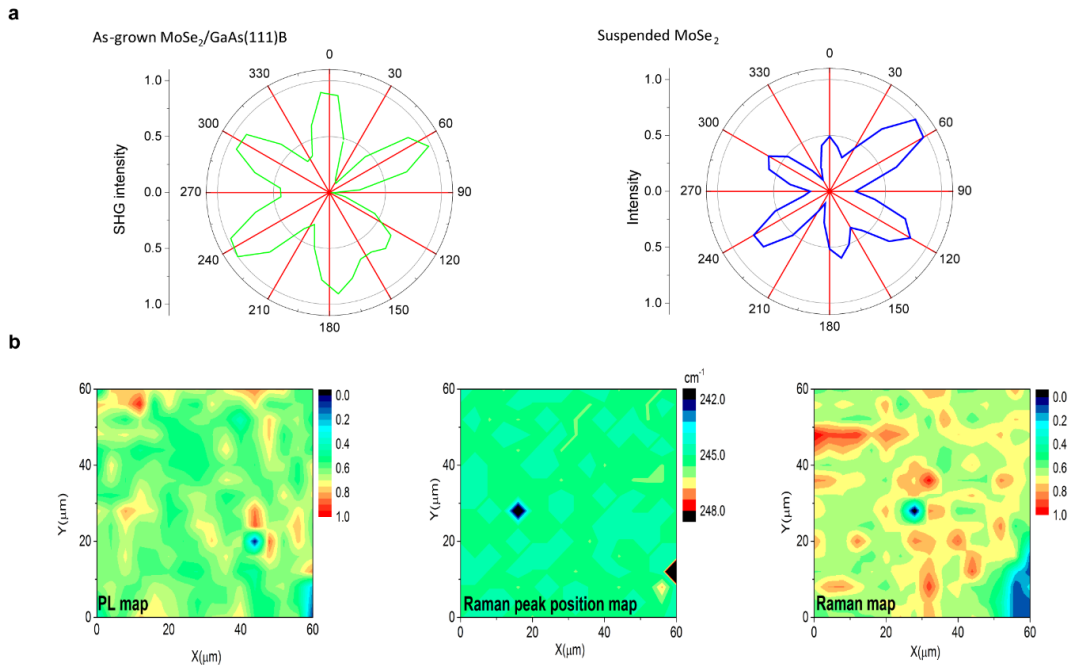


Figure S7. SHG and PL and Raman mappings of ML MoSe₂ grown at 530°C. (a) Polarization-dependent SHG plot of as-grown (left) and suspended MoSe₂ (right). (b) Normalized PL intensity mapping, Raman peak position and intensity mappings of transferred MoSe₂ on SiO₂ in a 60 × 60 μm² area.

In addition to the fact that we consistently observed only one set of FFT spots for MoSe₂ at different locations using STEM, we have also performed SHG spectroscopy as shown in Figure S7a. The polarization-dependent SHG plot of as-grown MoSe₂/GaAs(111)B on the left shows six-fold symmetry, which is characteristic of MoSe₂ in ML form exhibiting three-fold rotational symmetry. On the suspended MoSe₂ which was transferred on the TEM grid, the SHG results are reproducible and are in line with the STEM observations. The spot size of the focused laser here is 1-2 μm in diameter. Although the signals contributed from the GaAs substrate cannot be fully excluded, the as-grown sample and suspended MoSe₂ show similar results. The quality of large-area MoSe₂ transferred onto SiO₂ was examined by PL and Raman mapping. The spatial dependence of PL and Raman peak positions have been acquired by raster

scanning the sample over a $60 \times 60 \mu\text{m}^2$ region, and the results are shown in Figure S7b. Despite some intensity variations which might be due to polymer contamination or corrugations induced during transfer, the uniformity of ML MoSe₂ was confirmed.

5. MoSe₂ transistor measured in air and in vacuum

The MoSe₂ transistor before polymer electrolyte coating was first measured in air as shown in Figure S8a. There is only negligible back gate modulation effect observed in the device shown here and also in the other devices. The device was then measured in vacuum with the base pressure of $\sim 10^{-6}$ mbar, and the back gate sweep is shown in Figure S8b. Only transistors coated with polymer electrolyte can then show appreciable current modulation. We point out that the device shown here is the same one shown in Figure 3 in the main text.

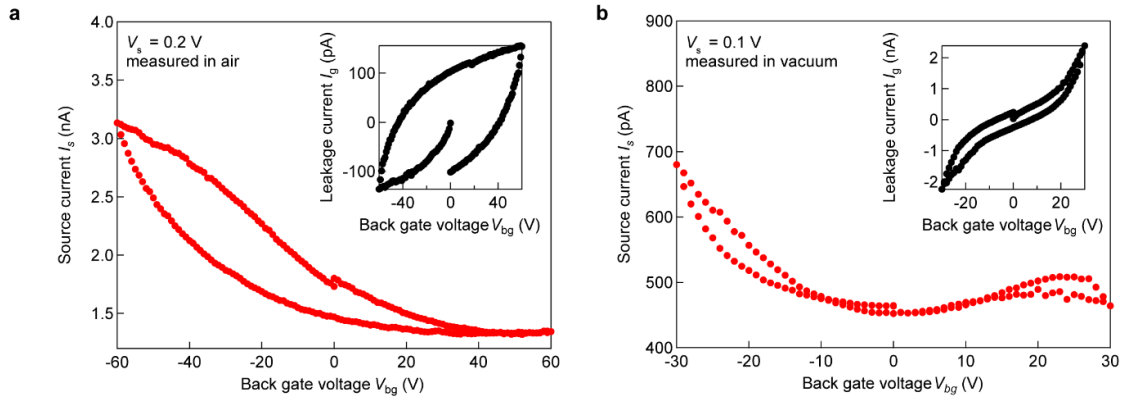


Figure S8. MoSe₂ transistor back gate sweep. Transistor was measured (a) in air and (b) in vacuum. Insets are the leakage current I_g for each sweep.

6. Field-effect mobility extraction

In order to extract the field-effect mobility, we cooled the four-contact transistor down to 200 K to freeze the polymer electrolyte at a given doping level. A back gate sweep was processed at each fixed doping level and the field effect mobility can be extracted from the equation $\mu_{\text{FE}} = (1/C_{\text{ox}}) \times (dG_{\text{sb}}/dV_{\text{bg}})$, where $C_{\text{ox}} = 1.28 \times 10^8 \text{ F cm}^{-2}$ is the geometric back-gate capacitance per unit area of 270 nm SiO₂. The back gate sweep for p and n sides are plotted in Figure S8a and Figure S8b, respectively. Inset in Figure S8b is the plot of contact resistance R_c vs. sheet resistance R_{sh} , showing that R_c only slightly decreases with the decrease of R_{sh} during the sweep. The summary of mobility is shown in Table S3 and implies that the low mobility values are due to the structural disorder and can be tuned in a limited range. The results lead us to investigate the VRH model discussed in the main text.

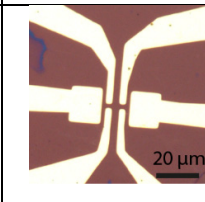
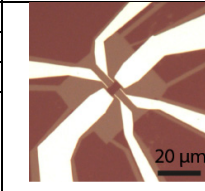
Sample No.	Transport regime	G_{sh} (μS) at 200 K ($V_{bg} = 0$ V)	Mobility ($\text{cm}^2 \text{V}^{-1} \text{S}^{-1}$)	Device image
Dev1	n	1.46	0.049 ± 0.001	
Dev2	n	1.49	0.055 ± 0.0009	
	p	1.50	0.28 ± 0.002	
	p	1.00	0.22 ± 0.002	
	p	0.30	0.048 ± 0.0004	

Table S3. Summary of field effect mobility extraction by back gate sweep at 200 K

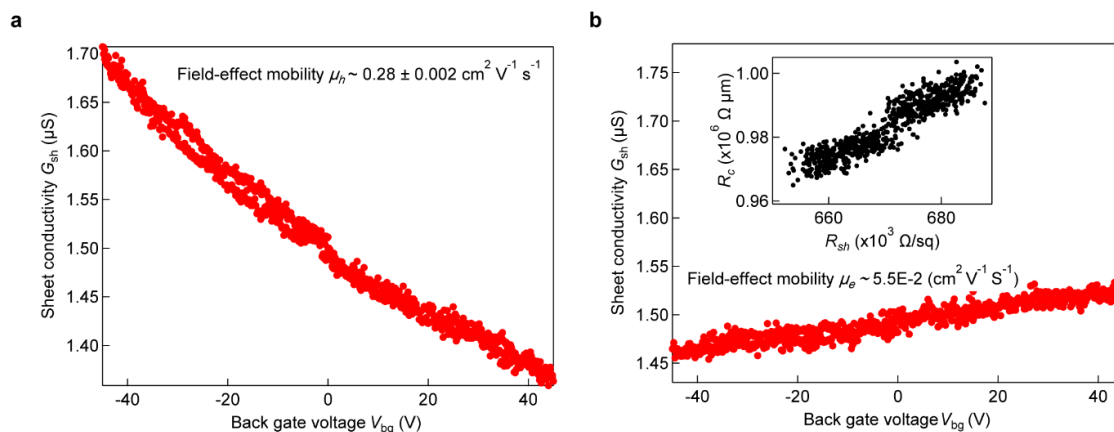


Figure S9. Field effect mobility extraction by back gate sweep at 200 K. (a) The back gate sweep at p -side at 200K. (b) The back sweep at n -side at 200K. The y-scale was fixed for both. The inset in (b) is the contact resistance R_c vs. sheet resistance R_{sh} in the same sweep.

7. Temperature cycling

For each cooldown, the EDLT was first stabilized at 280 K at a given V_{PE} . The polymer electrolyte PS-PMMA-PS:[EMIM]-[TFSI] completely freezes at 200 K which is evident by recording the constant G_{sh} while releasing the V_{PE} to 0 V (Figure S10a), i.e., the doping level was fixed at the given V_{PE} at 280 K and became insensitive to the change of V_{PE} at 200 K. The cooldown was processed at a rate of 0.5 °C/min to minimize the hysteresis, and at the end of each cooldown, we ramped up the temperature to 333 K (Figure S8b). The current level as shown became noisier above ~ 220 K, indicating the increase of electrolyte mobility towards the melting point. At ~ 260 K the current completely dropped to zero because the electrolyte was completely melted. The device was kept at 333 K for a while and then we ramped down the temperature to 280 K again to restart the cycle.

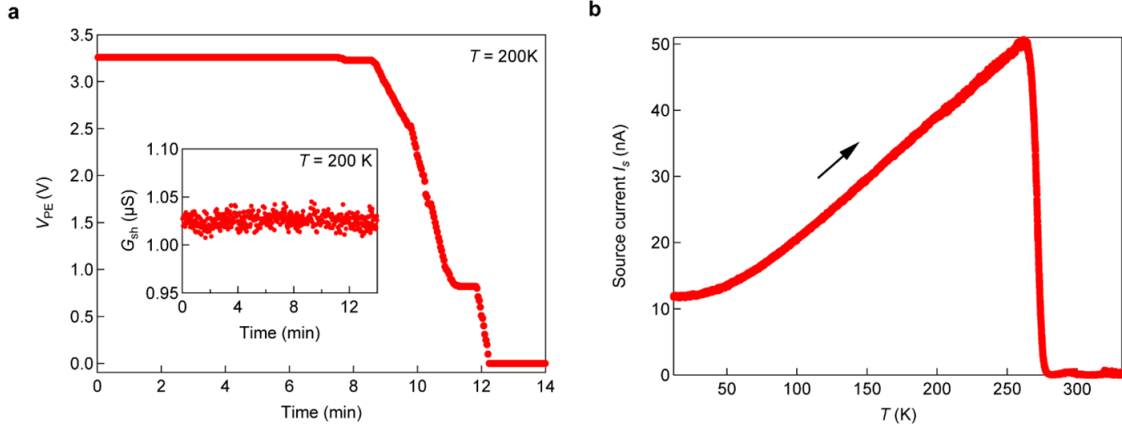


Figure S10. Temperature cycling. (a) The release of a given V_{PE} at 200 K after electrolyte was completely frozen. Inset is the G_{sh} recorded during the V_{PE} ramping-down showing a constant value. (b) The temperature ramping started at 12 K to 333 K. The black arrow represents the direction of the temperature ramp.

8. Variable range hopping in MoSe₂

The 2D-VRH model with the relation $G_{sh} \propto \exp[-(T_0/T)^{1/3}]$ where T_0 is the characteristic temperature, was applied here to explain the transport results. T_0 can be extracted by plotting $\ln G_{sh}$ vs. $T^{-1/3}$, as discussed in the main text. A higher T_0 represents a more disordered system and directly correlates to a shorter localization length ξ_{loc} which follows the equation $\xi_{loc} = \sqrt{13.8 / k_B D T_0}$, where D is density of states in the band of MoSe₂. The density of states D can be expressed as $D = g_s \times g_v \times m^* / \pi \hbar^2$, where g_s and g_v are spin degeneracy factor and valley degeneracy factor, respectively, m^* the effective mass of the charge carrier and \hbar the reduced Planck constant. The electronic band structure of free-standing ML MoSe₂ is shown in Figure S11 and was calculated within the same computational setup presented in Supplementary Note 3. We obtained holes and electrons effective masses (m_h^* and m_e^* , respectively) by fitting a parabola around the K point in the first Brillouin zone. Here we obtain the values of electron effective mass $m_e^* = 0.49 m_0$ and hole effective mass $m_h^* = 0.57 m_0$; $g_v = 2$ and $g_s = 1$ or 2 considering the cases of mixed ML and BL. The values of ξ_{loc} can then be extracted and are shown in the main text in Figure 4.

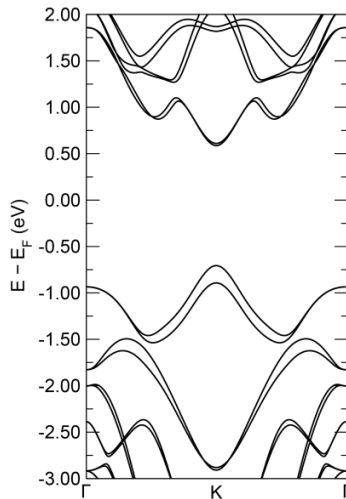


Figure S11. Electronic band structure of free-standing ML MoSe₂ from first-principles. Effective masses were extracted by fitting parabolas at the K point in the first Brillouin zone.

References

- (1) Jones, R. O. Density Functional Theory: Its Origins, Rise to Prominence, and Future. *Rev. Mod. Phys.* **2015**, *87*, 897–923.
- (2) Soler, J. M.; Artacho, E.; Gale, J. D.; García, A.; Junquera, J.; Ordejón, P.; Daniel Sánchez-Portal. The SIESTA Method for Ab Initio Order- N Materials Simulation. *J. Phys. Condens. Matter* **2002**, *14*, 2745.
- (3) Perdew, J. P.; Burke, K.; Ernzerhof, M. Generalized Gradient Approximation Made Simple. *Phys. Rev. Lett.* **1996**, *77*, 3865–3868.
- (4) Grimme, S. Semiempirical GGA-Type Density Functional Constructed with a Long-Range Dispersion Correction. *J. Comput. Chem.* **2006**, *27*, 1787–1799.
- (5) Björkman, T.; Gulans, A.; Krasheninnikov, A. V.; Nieminen, R. M. Van Der Waals Bonding in Layered Compounds from Advanced Density-Functional First-Principles Calculations. *Phys. Rev. Lett.* **2012**, *108*, 235502.